Article

Graphene oxide variations in NiGraf during OER: structural dynamics of nickel-based electrocatalysts for enhanced water electrolysis

Rocco Caliandro,[1]† Enrico Berretti,[2]† Maria V. Pagliaro,[2] Rosaria Ciriminna,[3] Vincenzo Mangini,[1] Cinzia Giannini,[1*] Alessandro Lavacchi,[2*] Mario Pagliaro[3*]

[1] Istituto di Cristallografia, CNR, via G. Amendola 1220, Bari 70126, Italy

[2] Istituto di Chimica dei Composti Organometallici, CNR, via Madonna del Piano 10, Sesto Fiorentino FI 50019, Italy

[3] Istituto per lo Studio dei Materiali Nanostrutturati - CNR, via U. La Malfa 153, 90146 Palermo, Italy

*Correspondence: cinzia.giannini@cnr.it, alessandro.lavacchi@cnr.it, mario.pagliaro@cnr.it

† These authors contributed equally to this work

SUMMARY

Alkaline water electrolysis, which relies on efficient and durable electrocatalysts made from earth-abundant metals like nickel for both hydrogen and oxygen evolution reactions, is a crucial energy storage technology for the transition to renewable energy. *In operando* techniques enabling the observation of active catalysts under relevant working conditions by monitoring the surface oxidation state and local atomic-structure transformation, can probe the active sites and promote fundamental understanding of the reaction mechanisms. In this study we present a new *operando* investigation of the electrocatalyst NiGraf by synchrotron X-ray Powder Diffraction and Pair Distribution Function. The structural changes in the crystal phases of this new metal organic alloy comprised of graphene oxide entrapped in nickel-based jamborite nanoparticles during voltammetry cycles in the OER range revealed a first reversible variation in the distance between GO planes during the reaction, and the subsequent reaching of the irreversible activation stage of the electrocatalyst. The technique, which couples Pair Distribution Function, Principal Component Analysis and *operando* electrochemistry is a new tool for the study of electrocatalysts in action.

Keywords: *Operando* X-ray diffraction, NiGraf, nickel, graphene oxide, electrocatalyst

INTRODUCTION

Operando and *in situ* studies are increasingly being applied to understand heterogeneous catalysts under real reaction conditions [1]. For example, advancements in high-brilliance and high-energy synchrotron X-ray sources, along with faster and more efficient detectors, offer opportunities to conduct *in situ*/*operando* Pair Distribution Function (PDF) experiments to investigate dynamic properties and time-dependent reaction process. Notably, electrochemical processes have leveraged synchrotron X-ray diffraction to optimize the design of more efficient batteries [2]. In general, PDF measurements provide structural information across different length scales, from the local atomic environment to the long-range structure, allowing the identification of contributions from different crystal phases. Unlike conventional diffraction methods, PDF does not require long-range order, making it ideal for the study of catalysts comprising disordered phases, including defect-rich small nanoparticles or amorphous phases. Various electrochemical cells for *in situ*/*operando* electrochemical/X-rays experiments have been developed [3,4,5] aimed at minimizing background X-ray scattering from the electrochemical solution and cell walls intersected by the X-ray beam. However, the main challenge of these experiments, which mainly monitor surface phenomena, lies in the low signal-to-background ratio and in the limited control over experimental conditions during the electrochemical reaction. Common issues include the formation of air bubbles at the electrodes and the predominance of bulk over surface X-ray scattering.

Nickel (alone or alloyed with iron in stainless steel) is the catalyst employed at both the cathode and the anode of commercial alkaline water electrolyzers [6], for the electrochemical Hydrogen Evolution Reaction (HER) [7,8] and Oxygen Evolution Reaction (OER) [9,10]. Its relatively high activity and far lower cost with respect to rare Platinum Group Metals (PGMs) make it the electrocatalyst of choice for the wider diffusion of alkaline water electrolysis (AWE) [11,12]. AWE is already used to manufacture around 1% of the global annual output of hydrogen. Using electricity from renewable energy sources, the technology will be widely deployed to produce solar (or "green") hydrogen for electric mobility and other end energy uses [13].

Nickel (II) species like oxides and hydroxides play a pivotal role during OER in alkaline environment. Metallic Ni turns to NiO during anodic polarization, which in turn transforms to α-$Ni(OH)_2$ (disordered phase) and β-$Ni(OH)_2$ (hexagonal, ordered phase), and subsequently to the relative oxyhydroxides, respectively γ-NiOOH (with a formal Ni oxidation state of 3.7), and β-NiOOH (with a formal Ni oxidation state of 3) [14]. Experimental results showed that these oxohydroxide species, especially the most disordered ones, are the prime responsible for the oxygen evolution catalytic activity of this material [14]. Their ratio in Ni-based materials, and the reversibility between Ni^{2+} and Ni^{3+} species, is strongly dependent on the electrocatalyst synthesis method [15]. In recent years, plentiful research efforts have been placed in increasing the activity of nickel, by coupling it with other elements and compounds [6,16]. Among these structures, Graphene Oxide (GO) has attracted particular interest due to its conductivity, high surface area and high chemical and mechanical stability [17,18]. In all these attempts, however, GO is used as support that is "decorated" with Ni-based catalytic species. A complementary approach was recently adopted with the introduction of NiGraf, a new molecularly doped metal comprised of GO 3D entrapped in nickel-based jamborite ($Ni(OH)_2$(NiOOH)) nanoparticles [19]. The catalyst is reproducibly synthesized by a simple one-pot procedure carried out in water starting from a Ni precursor salt, graphene oxide and sodium borohydride as reducing agent. Three different GO loading were tested, 0.2 %,1 % and 5 % (respectively NG 1, NG 2 and NG 3). The static PDF characterization of samples at various GO loads allowed the

identification of the crystal phases and their structural characterization, whereas electrochemical studies showed superior electrochemical performances for OER for samples with added GO [19]. It was observed that the addition of GO induces an order-disorder transition, resulting in a reduction of crystallinity of the jamborite.

Still, several questions remain unanswered: how do the electrochemical properties of the GO@Ni catalysts correlate with their structural features? And how do the two crystal phases interact during the electrochemical process, potentially leading to correlated structural changes? To address these inquiries, we have designed and developed a novel electrochemical cell for *operando* PDF studies and conducted dedicated synchrotron experiments on NiGraf. The substantial volume of data collected were processed using Principal Component Analysis (PCA) to reduce dimensionality and extract trends in data. PCA was applied both to X-ray powder diffraction profiles (XRPD) and PDF profiles, and results interpreted within the framework of Modulation Enhanced Diffraction (MED), a theoretical framework that has been developed to interpret the X-ray diffraction signal from systems subjected to external stimuli [20,21].

2. RESULTS AND DISCUSSION

2.1 Development of the Electrochemical Cell for *operando* PDF measurements

The design of the electrochemical cell is derived from a cell previously adopted for X-ray Absorption Spectroscopy (XAS) experiments [22, 23, 24], to fit with the typical geometry of synchrotron X-ray diffraction (XRD) experiments [2] (Figure S1). The experiment design criteria were focused on decreasing the background scattering from both the liquid electrolyte and the cell materials. For these reasons, the volume of water solution crossed by the X-ray beam was minimized, moving away the working and reference electrodes from the beam line. In addition, kapton windows were placed where the primary and scattered beams pass through the cell. Kapton is widely used in X-ray experiments due to its high resistance to radiation, relatively low absorption, and very low angle diffraction peaks. PDF measurements necessitate the collection of photon at wide scattering angle, to enhance the momentum transfer integration. To fulfill this requirement, the position of the sample was shifted from upstream (Figure S1b) to downstream (Figure 1a) with respect to the beam and the rear wall flared to avoid interference with photons scattered at wide angles (Figure 1a). This redesigned cell utilizes plexiglass (PMMA) as bulk material (Figure 1b). The housing for the sample and the electrolyte solution is accessible via a lid closed with screws, which prevent liquid leakage. Two grooves to hold the counter (CE) and reference (RE) electrode were positioned in the upper part. The base substrate for the working electrode (WE) was made by a thin (200 μm) carbon paper sheet, which was squeezed between the intermediate cell element and the flared support (Figure 1-b) in order to prevent solution leakage. A 1 mm pinhole was punched on the carbon paper, to be placed on the center of the hole on the flared cell element. The purpose of the pinhole was dual: *i*) to enable electrical contact between the WE and the electrocatalyst ink dropcasted on the carbon paper substrate, and *ii*) to decrease the background signal during the X-ray experiment, by targeting the center of the pinhole with the beam. To facilitate sample replacement during measurements, a practical solution was devised: the centering base, fixed to the work table in the beamline as shown in Figure 2, is kept separate from the electrolytic cell. The latter can be easily assembled and disassembled from the base by inserting it into a groove on the base, enabling fast positioning of the cell body without further alignment.

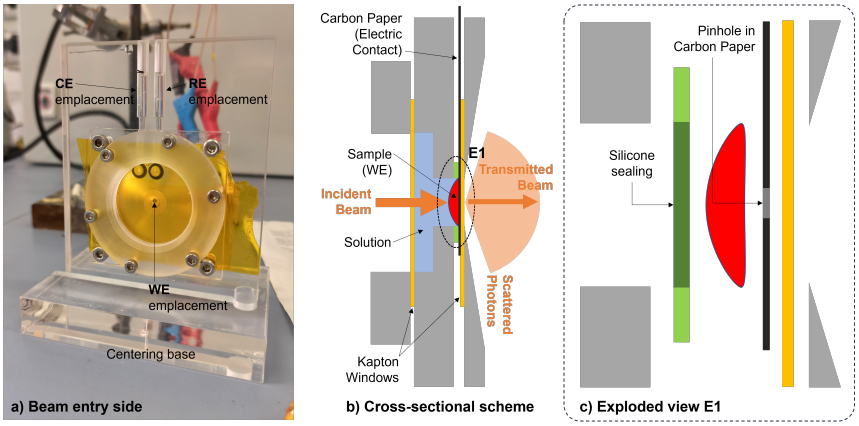

Figure 1. Front (a) and side cross-sectional (b) views of the electrochemical cell developed for operando Pair Distribution Function experiments; (c) exploded view (E1) of the WE assembly particular.

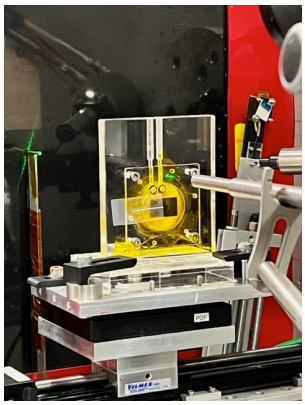

Figure 2. The electrochemical cell mounted in the experimental setup of the beamline ID-28-2 at BNL.

2.2 Calibration of the electrochemical cell

Empty cell measurements were conducted to refine the cell design and establish a reference for background subtraction. Figure 3 illustrates the XRPD profiles collected at two different positions of the cell in a plane perpendicular to the primary X-ray beam, relative to the center of the pinhole (Figure 3, red) and to the carbon paper (Figure 3, black). Notably, peaks at q = 0.8 Å^{-1} and q = 1.3 Å^{-1} were consequently attributed to the presence of the carbon paper on the beam path. To minimize this effect, we fixed the position of the cell base at the beginning of the experiment and signed the exact position of the mobile part of the cell, to retain the same position of the hole with respect to the beam when changing the catalytic samples.

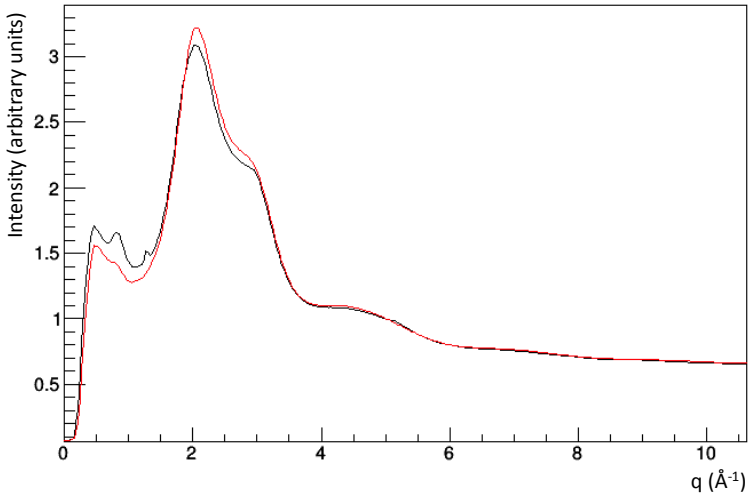

Figure 3. X-ray powder diffraction profiles measured in two different positions (black and red curves) of the electrochemical cell without sample.

The next step was to acquire the PDF measurements of the complete electrochemical cell under open circuit potential (OCP), by using the sample with higher crystallinity (NG1) as target. To assess the impact of the *operando* configuration on the PDF profile calculation, we compared the *in situ* OCP result with the ones from the measurement of the same sample *ex situ* performed using a glass capillary as a sample holder. For the elaboration of both measurements, a background subtraction was performed (the subtraction of the empty capillary for the *ex situ* measurement). A PCA comparison of the PDF profiles generated with and without background subtraction (Figure 4a) reveals significant differences between profiles obtained *ex situ* and *in situ* OCP conditions. Background subtraction has a minor effect on *ex situ*, with representative points 0 and 1 spread along PC2, which accounts for only 10.3% of the total data variance. In contrast, background subtraction applied to the *in-situ* OCP measurements produces a notable effect, with representative points 2 and 3 separated along PC1, which accounts for 82.7% of the total data variance. Consequently, the background-subtracted *in situ* PDF profile (3) closely resembles those calculated in static conditions (0 and 1), while the original *in situ* profile lies outside this cluster. The significant effect of background subtraction in *in situ* OCP measurements (Figure 4b) is attributed to the considerably higher scattering power of materials encountered by the X-ray beam passing through the cell (electrolytic solution, kapton windows, carbon paper) compared to the empty glass capillary.

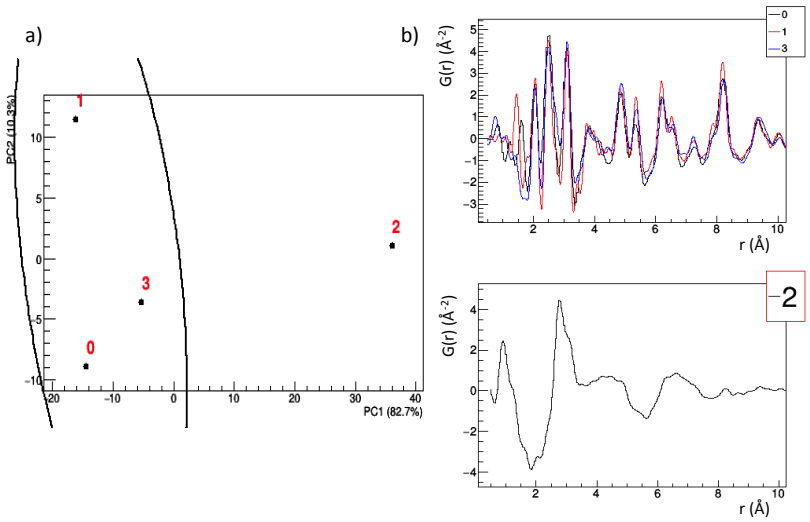

Figure 4. Principal component analysis (PCA) comparison among PDF profiles calculated from static measurements with (1) and without (0) background subtraction and from *operando* measurements with (3) and without (2) background subtraction. a) Scores plot of the first two principal components: PC1 and PC2. Each point in this space represents a PDF profile. The fraction of total data variance explained by the principal components is reported in parenthesis along the axes. The ellipse shows the result of a hierarchical clustering procedure applied on the points in the scores plot. b) PDF profiles grouped according to the clustering results.

A closer examination of PDF generation in static and *in situ* setups is presented in Figure S2, where the measured XRPD profiles are overlaid to those used as background, the reduced total scattering structure function $F(q)$ and the PDF function $G(r) = \frac{2}{\pi}\int_{q_{min}}^{q_{max}} F(q)\sin(qr)dq$ are plotted. Despite the markedly different shapes of the profiles measured under static and *in situ* conditions, the corresponding $F(q)$ profiles, calculated after background subtraction, exhibit remarkable similarity. The primary difference lies in the extent of the useful q range: the static $F(q)$ profile retains significant values up to q = 23 Å^{-1}, whereas the *in situ* profile is limited to q < 17 Å^{-1} due to fluctuations occurring at higher momentum transfer values. Despite these differences, the resulting PDF profiles are quite similar, as previously indicated in Figure 4. The parameters used for PDF generation are listed in Table S1.

2.3 *Operando* analysis of sample NG1

Voltage was applied at 50 mV/min rate between 1 and 2 Volt *vs.* RHE. Thus, a full voltammetry cycle took about 40 min. The voltammetric curve for the first cycle is reported in (Figure 5). Throughout the voltammetry experiment, X-ray Powder Diffraction (XRPD) profiles were continuously acquired, with a total of 39 measurements within a voltammetry cycle.

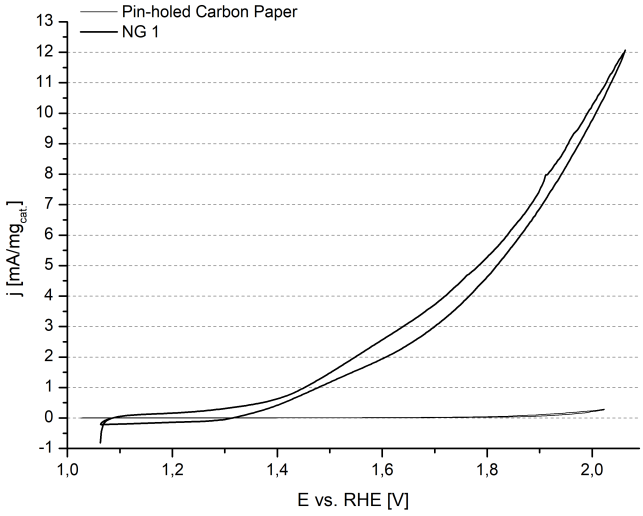

Figure 5. Voltage applied and current measured in the cyclic voltammetry experiment carried out on NiGraf sample NG1.

The data matrix comprised of the 39 measurements underwent PCA processing to detect trends with high sensitivity. This fast processing was also employed during the experiment's execution, to monitor system responses and make decisions regarding further measurements. Despite seemingly unchanged profiles from one measurement to another (Figure 6a), PCA decomposition revealed well-defined monotonic trends in the first principal component (PC1), explaining 74.7% of the total data variance. This trend was accompanied by a quadratic trend in the second principal component (PC2), explaining 17.2% of the total data variance (Figure 6b). Additionally, PC4, explaining only 2.1% of the total data variance, exhibited a trend strongly correlated to the applied voltage. The loadings plot (Figure 6d) can, in principle, be interpreted as the XRPD profile associated to each PC trend. However, due to the nanometric size of the NG1 crystallites resulting in broad XRPD peaks, and the experimental setup optimized for PDF measurements limiting the angular resolution of XRPD profiles, the information contained within the XRPD profiles (and consequently the loading plots) is of limited utility. To overcome this limitation, we pursued two approaches:

1) to enhance peak separation peaks, we conducted the *operando* measurement again using a setup optimized for XRPD measurements, by the detector placed further away from the sample. However, under these conditions, the results of the PCA, as depicted in Figure S3, revealed higher fluctuations in the score values. This suggests the presence of random differences among sequentially collected measurements, likely attributable to extended path (1411 mm) travelled by scattering photons before reaching the detector. This extended path severely impedes the detection of trends in data across the *operando* measurements.

2) to enhance interpretability of the PCA loadings, we processed the PDF profiles instead of the XRPD ones. This approach focused on the potential for loading values to contain information about the local structure of the material. However, a notable disadvantage of this approach is that the input for PCA is derived from

processing steps (such as the calculation of the normalized total scattering function and sine Fourier transformation [11]) rather than directly measured data.

Results shown in Figures S4 and S5 indicate a significant signal only for the first principal component (PC1). Notably, the shape of the loadings corresponding to subsequent component lacks physical meaning: their characteristic periodicity in *r* space is close to $2\pi/Q_{max}$, which corresponds to the expected value for ripple artefacts arising from to the finite Q-range [26]. Additionally, their envelope does not exhibit a decreasing trend, typical for a PDF [26]. This observation remains valid whether the background is subtracted from the signal (Figure S5) or not (Figure S4).

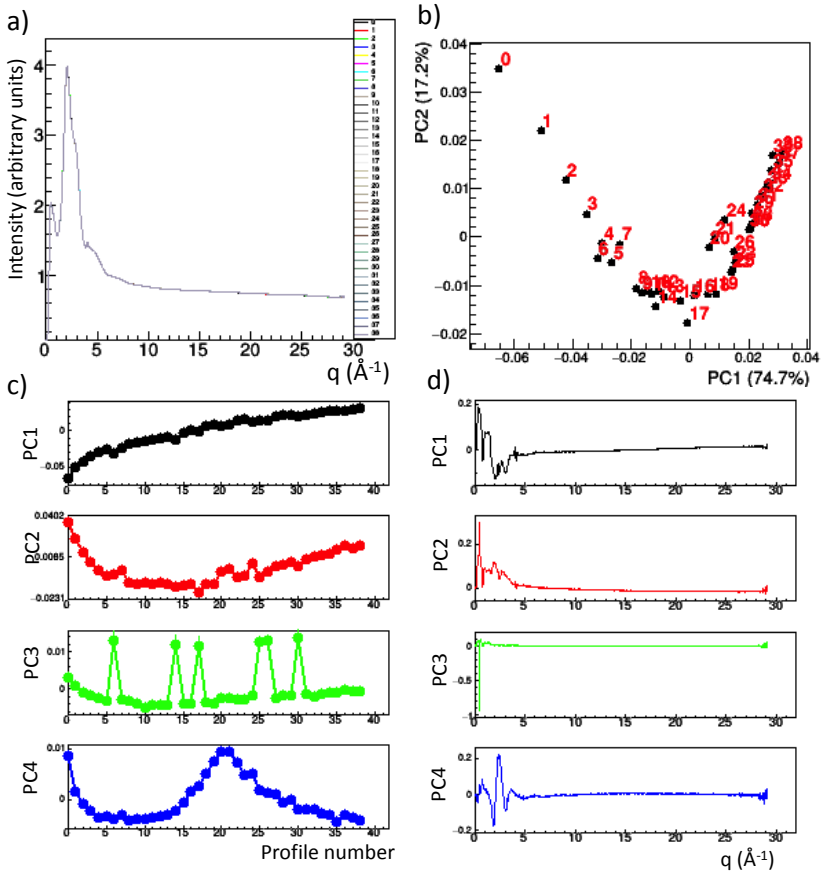

Figure 6. PCA comparison among XRPD profiles measured operando with a setup optimized for PDF measurements for NiGraf sample NG1. a) XRPD profiles superposed. b) Scores plot of the first two principal components. The percentage of data variance explained by each component is reported on its axis. c) Scores of the first 4 principal components. d) Loadings of the first 4 principal components.

2.4 *Operando* analysis of NiGraf sample NG2

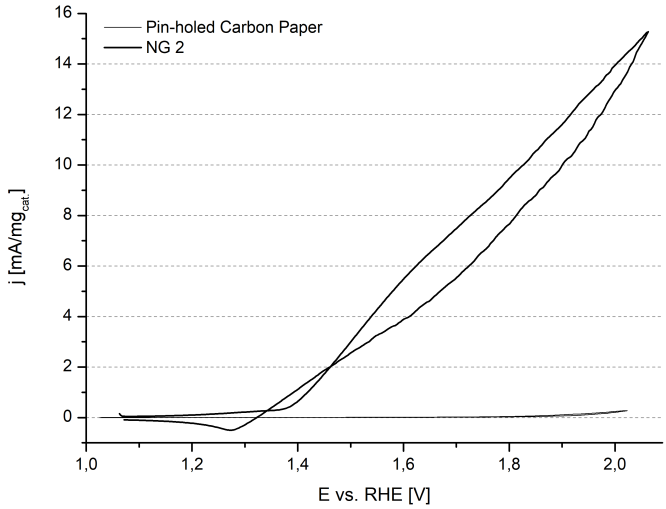

Figure 7 Voltage applied and current measured in the cyclic voltammetry experiment carried out on NiGraf sample NG2.

The results of the first cycle of the voltammetry/PDF experiment conducted on NiGraf sample NG2 are displayed in Figure 7. The PCA comparison of the measured XRPD profiles shows a distinct quadratic relationship between the second component, explaining 2.6% of the total data variance, and the first component, explaining 96.6% of the total data variance (Figure 8b). Similar to sample NG1, PC1 scores shows a monotonic trend, but the corresponding loadings appear inverted. It should be noted that both the scores and loadings carry a sign ambiguity, and only the product *(Scores* × *Loadings)* has a definite sign. Hence, the parabola shown in Figure 8b has a concavity pointing downwards, whereas it points upwards in Figure 4b. Similarly to NG1, XRPD measurements collected in the optimized XRPD setup do not yield significant results (data not shown). However, the PCA applied to PDF profiles proves to be more informative than in the NG1 case (Figure 9). Here, a clear quadratic relationship between PC1 and PC2 scores can be seen in Figure 9b, and the trends in score values depicted in Figure 9c mirror those in the XRPD case (Figure 8c), albeit with opposite signs. Higher principal components are deemed insignificant, according to criteria mentioned previously.

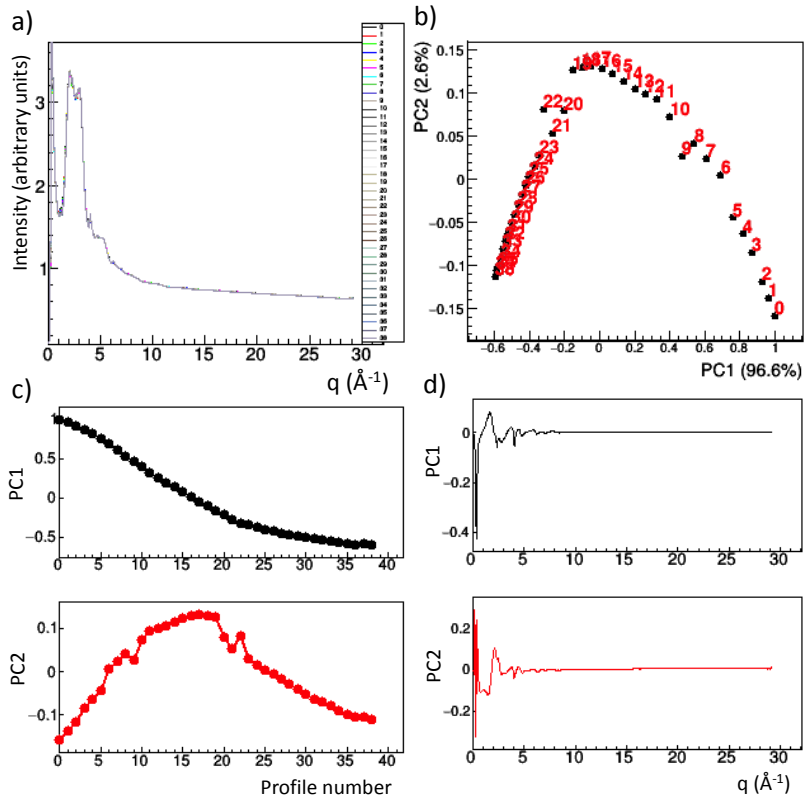

Figure 8 PCA comparison among XRPD profiles measured operando with a setup optimized for PDF measurements for NiGraf sample NG2. a) XRPD profiles superposed. b) Scores plot of the first two principal components. The percentage of data variance explained by each component is reported on its axis. c) Scores of the first 2 principal components. d) Loadings of the first 2 principal components.

Despite the significant modification of the PDF profile resulting from background subtraction (Figure 9a *vs.* Figure S6a), it has a minor effect on PCA results. Specifically, the score values associated with the first two principal components (Figure 9b,c vs Figure S6b) are very similar, while the loading values exhibit similarity only for PC1, but are rather different for PC2, which explains only a few percent of the total data variance (Figure 9d *vs.* Figure S6d). This discrepancy arises because background subtraction is consistently applied to all the PDF profiles, resulting in only small-scale variations from one profile to another. However, PCA emphasizes differences among profiles, thus neglecting constant terms introduced by background subtraction.

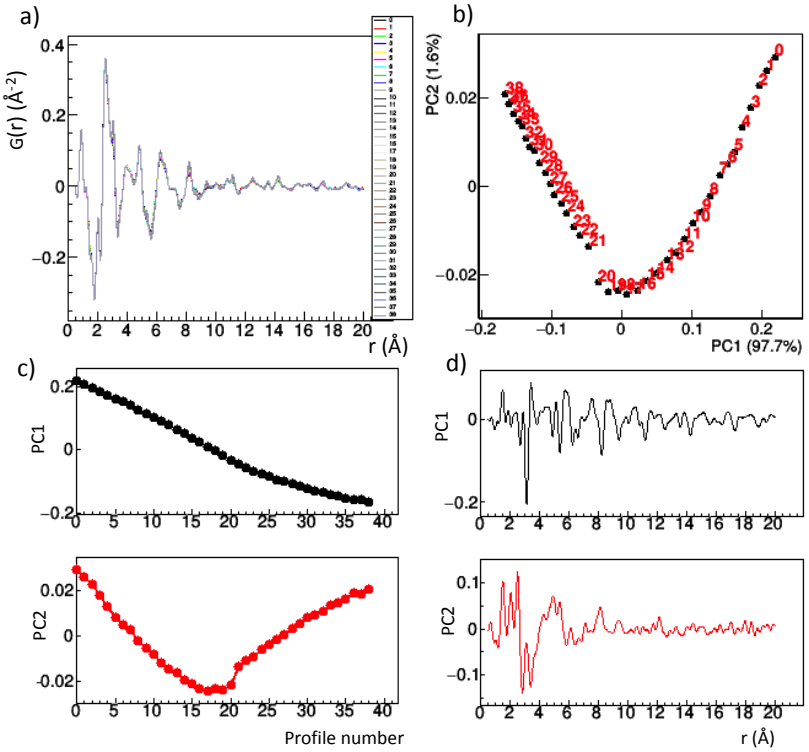

Figure 9 PCA comparison among PDF profiles without background subtraction obtained from *operando* measurements on NiGraf sample NG2. a) PDF profiles superposed. b) Scores plot of the first two principal components. The percentage of data variance explained by each component is reported on its axis. c) Scores of the first 2 principal components. d) Loadings of the first 2 principal components.

2.5 *Operando* analysis of NiGraf sample NG3

The outcomes of the first voltammetry/PDF experiment conducted on NiGraf sample NG3 are reported in Figure 10.

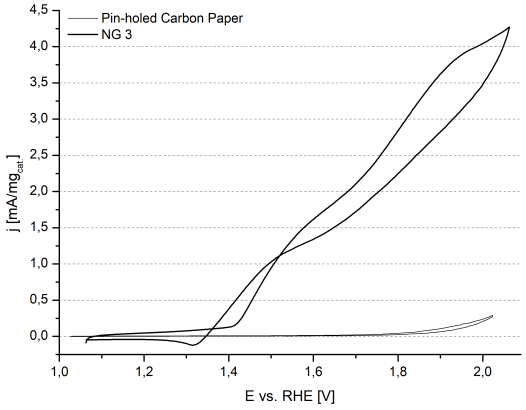

Figure 10 Voltage applied and current measured in the cyclic voltammetry experiment carried out on NiGraf sample NG3.

The PCA comparison of XRPD profiles is shown in Figure 11. Notably, a quadratic trend of PC2 scores with respect to PC1 scores is still observed, although deviations from this trend are observed for the last measurements of the first voltammetry cycle.

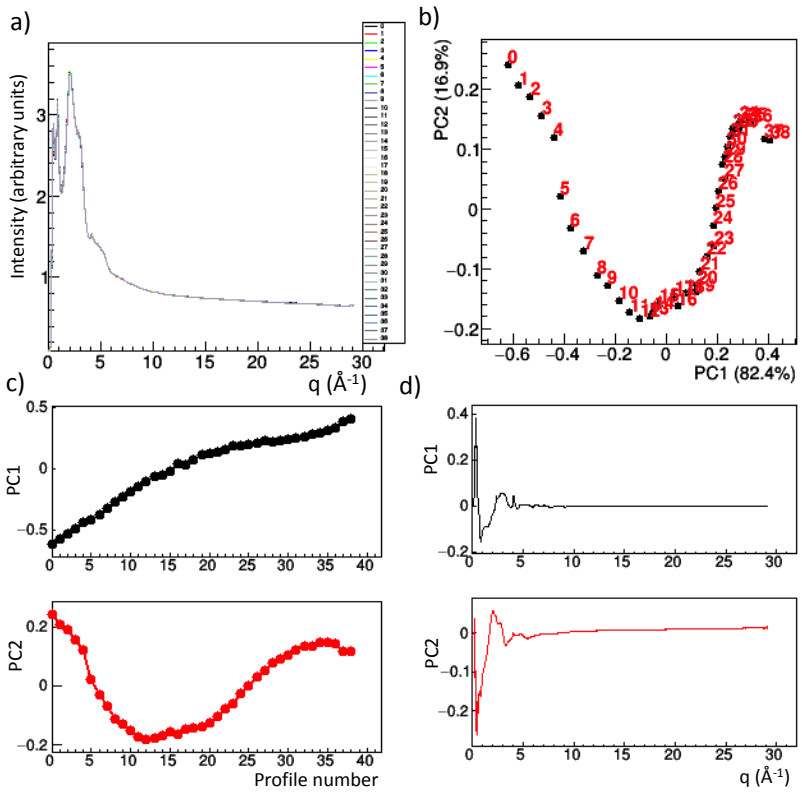

Figure 11 PCA comparison among XRPD profiles measured *operando* with a setup optimized for PDF measurements for NiGraf sample NG3. a) XRPD profiles superposed. b) Scores plot of the first two principal components. The percentage of data variance explained by each component is reported on its axis. c) Scores of the first 2 principal components. d) Loadings of the first 2 principal components.

The PCA applied to PDF profiles yields similar trends in scores to those obtained for XRPD profiles only when background is not subtracted (Figure 12). Instead, background-subtracted PDF profiles decomposed by PCA do not exhibit the expected quadratic relationship between PC1 and PC2 scores as predicted by the MED theory (Figure S7). Since PCA is a blind decomposition driven by the direction of maximum variability in the data, such discrepancies can arise. To address this issue, a constrained decomposition method called Optimal Constrained Component Rotation (OCCR), can be employed [27,28]. In OCCR, the two principal components determined by PCA, which are necessarily orthogonal to each other, are independently rotated within a global optimization search. This search uses a cost function that rewards solutions for which eq. (1) is fulfilled. Specifically, the cost function is defined as the Pearson correlation coefficient between the second (rotated) score and the square of the first (rotated) score) [27]. The best rotation values found were φ =-0.970 rad and ψ=-0.097 rad, with an increase of the cost

function from 0.487 to 0.968. The scores and loadings obtained by OCCR are shown in Figure S8.

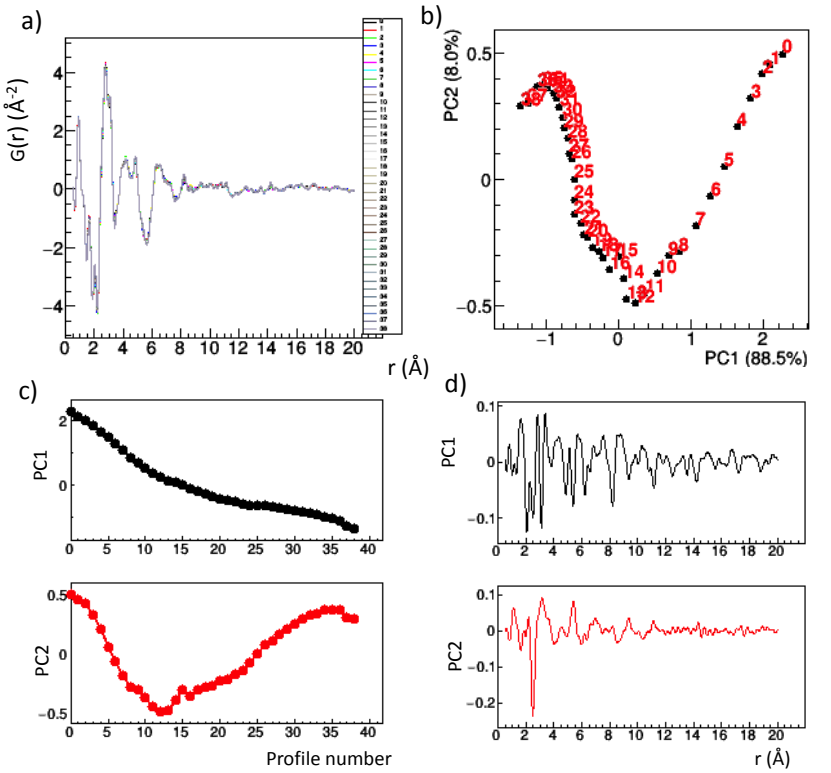

Figure 12 PCA comparison among PDF profiles without background subtraction obtained from *operando* measurements on sample NG3. a) PDF profiles superposed. b) Scores plot of the first two principal components. The percentage of data variance explained by each component is reported on its axis. c) Scores of the first 2 principal components. d) Loadings plot of the first 2 principal components.

2.6 Electrochemical considerations

From a qualitative point of view, we were able to observe for each of the three samples the typical features relative to Ni electrochemistry. Peaks attributable to Ni^{2+} <-> Ni^{3+} transition are in fact visible in the 1.25-1.45 V potential range [29], while the onset for OER floats around 1.4 V. While we were able to acquire a single scan for NG1, we performed two consecutive electrochemical cycles for NG2 and NG3, as reported in Figure 13. The lower performances of sample NG3 with respect to NG1 and NG2 were attributed to a loss of catalyst mass during the conditioning cycles, due to the production of O_2 gas, which in turn mechanically detaches some catalyst powder particles from the surface of the electrode. Interestingly, the same catalyst manifested an important change in the CV profile between the two subsequent cycles. The voltammetry plot in Figure 13 (right chart) shows an important increase of both peaks related to Ni^{2+} <-> Ni^{3+} transition.

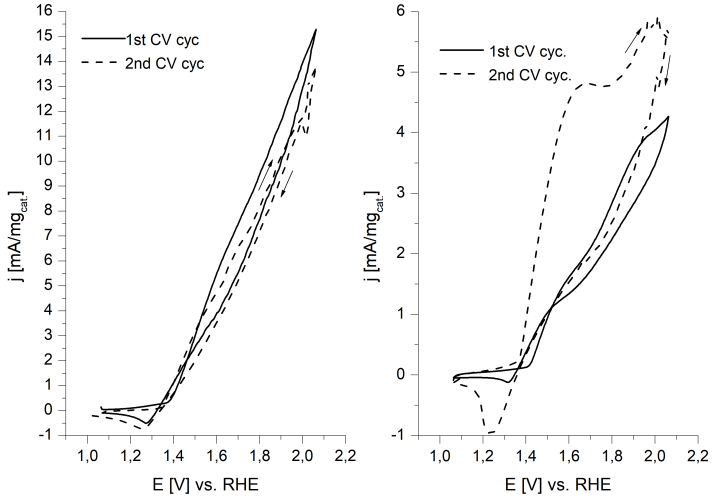

Figure 13. Consecutive cyclic voltammetry for NG2 (left) and NG3 (right) NiGraf catalysts.

2.7 Two-cycles data

For samples NG2 and NG3, we acquired the same series of PDF profiles for two consecutive cyclic voltammetries. Despite the quality of the second cycle, these data can be used to correlate the electrochemical system response (current) with that observed by XRD. Previous analysis on the first voltammetry cycle has shown that: *i*) the trend of PCA scores is similar in XRPD and PDF data, *ii*) PDF data provides the opportunity to interpret loadings value in terms of changes in the local structure, and *iii*) background subtraction in PDF could introduce differences among profiles that alter the scores value. For these reasons, we opted to use PDF profiles without background subtraction for developing the analysis of the two-cycles data. PCA applied to these data from NG2 is shown in Figure ***14***. The 3D scores plot, where the scores in the first three principal components are compared (Figure ***14***a), shows that the MED quadratic relationship [eq. (1)] retains its validity between different score value planes. In the first voltammetry cycle, it holds between scores PC1 and PC3, while in the second cycle it is valid between PC2 and PC3. Similarly, if the 3D score plot PC1-PC3-PC4 is considered, the quadratic relationship holds between PC1 and PC4 in the first cycle, and between PC3 and PC4 in the second cycle (data not shown). A rigorous application of the MED criterion, which requires a well-defined plane between two principal components where the quadratic relationship holds, therefore is not possible. Nevertheless, we observe that the trend of the PC3 and PC4 scores shown in Figure ***14***b correlates with that of the current shown in Figure 7 for the first voltammetry cycle. Conversely, the instability of the electrochemical cell encountered in the second cycle, probably due to the formation of air bubbles, introduces differences in the collected XRD data that disrupt the continuous trend of the PCA scores. Notably, the loading values associated with PC3 or PC4, which according to the above arguments can be considered as signals related to active atoms, both exhibit the highest peak at 2.5 Å (Figure ***14***c).

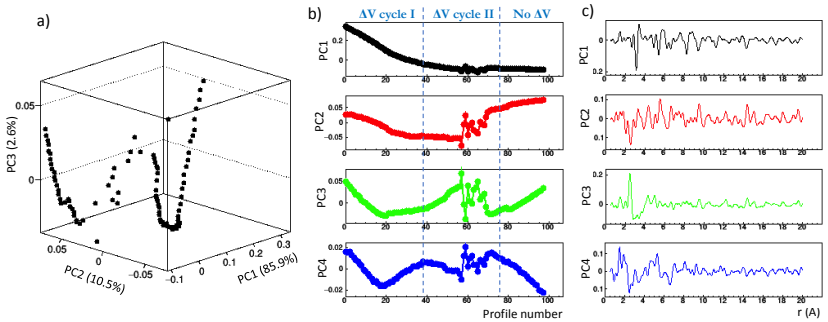

Figure 14 PCA comparison among PDF profiles without background subtraction obtained from *operando* measurements in two voltammetry cycles on NiGraf sample NG2. a) Scores plot of the first 3 principal components. The percentage of data variance explained by each component is reported on its axis. b) Scores of the first 4 principal components. Dashed lines denote the correspondence with the voltammetry cycles. c) Loadings of the first 4 principal components.

Similar results are observed for the two-cycle data collected for NG3 (Figure *15*). The pertinent MED plane in this case is formed by PC1 and PC2, at least in the first voltammetry cycle (Figure *15*a). Here, a distinct correlation between the PC2 scores shown in Figure *15*b and the trend of the current shown in Figure 10a is evident in both cycles. Additionally, the trend of PC2 scores becomes constant towards the end of the second cycle, when the potential is halted while XRD measurements are still being collected. Consequently, the PC2 component can be linked to the system response attributed to active atoms, and its loading values (Figure *15*c) still have a large peak at 2.5 Å, similar to the NG2 sample.

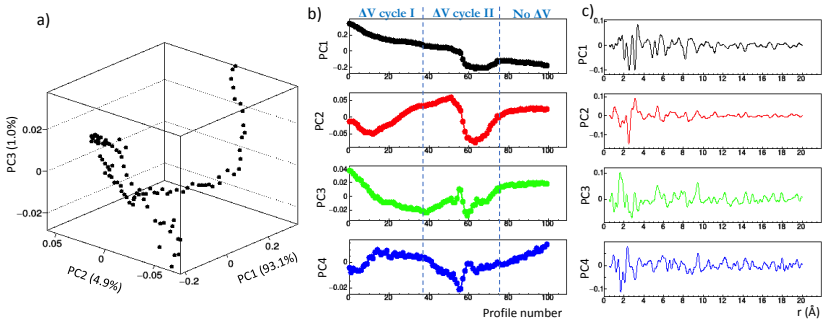

Figure 15 PCA comparison among PDF profiles without background subtraction obtained from *operando* measurements in two voltammetry cycles on sample NG3. a) Scores plot of the first 3 principal components. The percentage of data variance explained by each component is reported on its axis. b) Scores of the first 4 principal components. Dashed lines denote the correspondence with the voltammetry cycles. c) Loadings of the first 4 principal components.

2.8 Structural interpretation of the system response to the electrochemical stimulus

The static PDF profiles of the three NiGraf samples considered in this study have been structurally interpreted: we identified the Ni and GO crystal phases present in the samples using COD numbers 9012316 (jamborite) and 9012236, respectively [19]. The PDF profiles calculated from these phases are depicted in Figure 16, alongside relevant views of the crystal structures. The same fitting parameters previously reported [19] were employed in the PDF calculations. Notably, the highest peaks in the PDF profile are located within 3.5 Å. Peaks at 1.5 Å and 2.5 Å originate from the GO phase, while those at 2.0 Å and 3.1 Å from the jamborite phase. Thus, they offer a unique fingerprint of the two crystal phases present in the samples. Based on this outcome, we can interpret the loading values obtained through model-free analysis of *operando* data in terms of contribution from individual crystal phases and their possible changes.

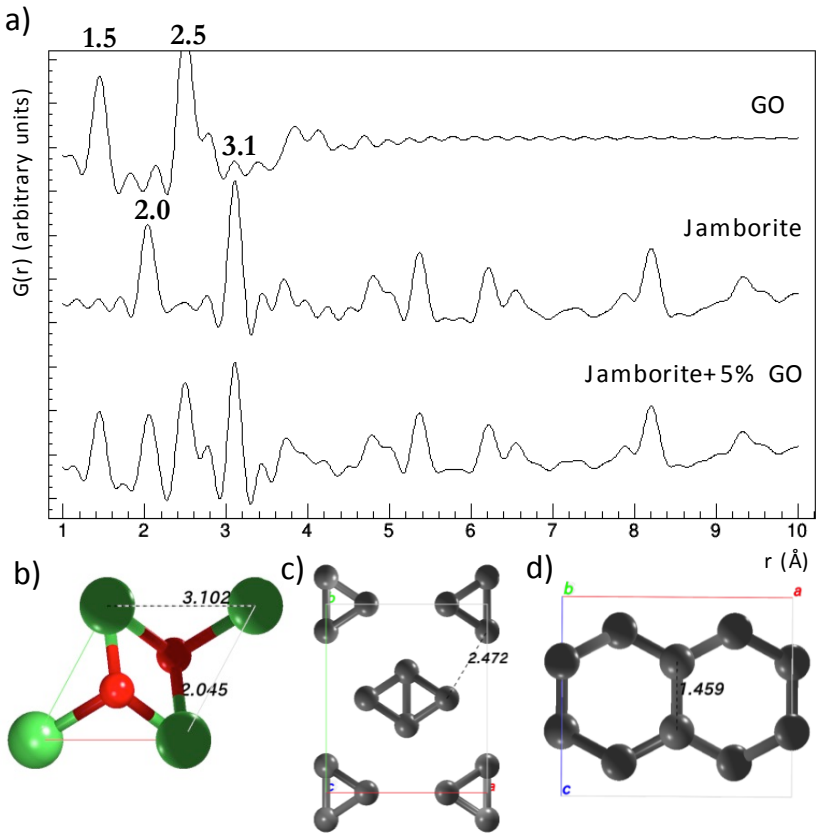

Figure 16 a) PDF profiles calculated from the crystal phases identified in sample NG3: Ni phase COD 9012316 (jamborite) and GO phase COD 9012236. b) View along the c axis of the Ni crystal phase, with Ni and O atoms colored in green and red, respectively. c) View along the c axis of the GO phase. d) View along the b axis of the GO phase. Relevant distances are indicated in Å in the crystal structures and on the corresponding PDF peaks.

We started with a study of the full stack of PDF data, to determine the major changes in distances throughout the whole voltammetric cycle. Given the stronger correlation between electrochemical and XRPD response observed for the NiGraf

material NG3, we focused on PC1 and PC2 loadings obtained by PCA applied to the PDF profiles (without background subtraction) collected during the two voltammetry cycles on this sample. We aimed to fit these loadings with pure-phase calculated PDF profiles. In the fitting model in eq.2, $G_{Jam}(r)$ and $G_{GO}(r)$ respectively are the PDF profile of the jamborite and GO crystal phases, and *a* and *b* are scale factor considered as free parameters in the fitting (they can be also negative, to account for intrinsic PCA sign ambiguity):

$$G(r) = aG_{Jam}(r) + bG_{GO}(r) \qquad (2)$$

Fitting results are shown in Figure 17, with $G_{Jam}(r)$ and $G_{GO}(r)$ fitted separately on the loadings profiles, and relative parameters *a* and *b* reported in Table S1.

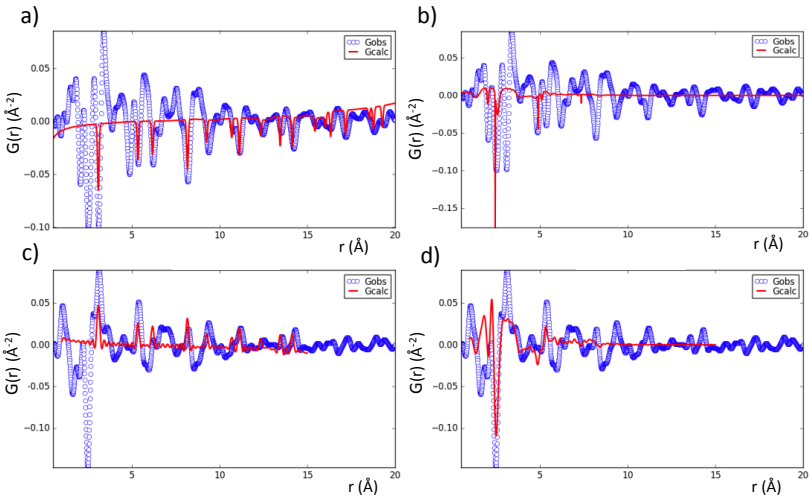

Figure 17 Loading values obtained by PCA applied to PDF profiles without background subtraction from *operando* measurements in two voltammetry cycles on NiGraf sample NG3 (blue circles) fitted with Jamborite (COD 9012316) and GO (COD 9012236) (red lines) crystal structures. a) PC1 loadings fitted with the Jamborite phase only; b) PC1 loadings fitted with the GO phase only; c) PC2 loadings fitted with the Jamborite phase only; b) PC2 loadings fitted with the GO phase only.

Figure 17 shows that the GO phase explains many more features of the PC1 and PC2 values, if compared to Jamborite, while in PC2 (panels c and d) the two crystal structures appear with opposite signs, indicating opposite dynamic trends during the oxidation and reduction processes. The main contribution to the loadings profile comes from the interatomic distance of 2.5 Å (Figure 17d), which corresponds to the separation between nearby GO entities that develop along the *c* axis (Figure 16c). Conversely, the distances related to the GO hexagonal carbon ring along the *b* axis (Figure 16d) remain nearly unchanged. The role played by the Ni phase associated with oxidation-reduction cycles appears therefore to be minor. This could be attributed to the minimal effect of changes in the Ni oxidation state on varying the first-shell interatomic distances. A similar result is found for the NG2 sample when considering PC1 and PC3 loadings. The fitting parameters presented

in Table S2 corroborate the predominant role of the GO phase, particularly the peak at 2.5 Å (

Figure *14*c) in determining the PC3 loadings. This indicates the contribution to the component related to active atoms.

The loading values obtained from the PCA applied to single voltammetry cycles - as shown in Figure S4 for NG1, Figure 9 for NG2 and Figure 12 for NG3 - are compared in Figure 18 by means of PCA. Only the significant principal components were considered, thus rejecting the components higher than 1 for NG1 and higher than 2 for NG2 and NG3. The shape of the loadings profiles in Figure 18a, and the arrangement of their representative points in Figure 18b, indicate that NG2 and NG3 PC1 loadings are very similar, and differ from the PC2 loadings of samples NG2 and NG3, as well as from PC1 loadings of sample NG1. The main common feature of the first cluster of points (NG2 and NG3 PC1 loadings) is a significant (negative) PDF peak at 3.1 Å, which corresponds to the Ni-Ni distance in the jamborite phase (Figure 16b). On the other hand, the main feature in the second cluster of points (NG2 and NG3 PC2) is a substantial (negative) PDF peak at 2.5 Å, which is associated with the distance among C columns along the *c* axis in the GO phase (Figure 16c). The PC1 loadings of NG1, despite having a characteristic peak at 3.1 Å, are more akin to the PC2 points.

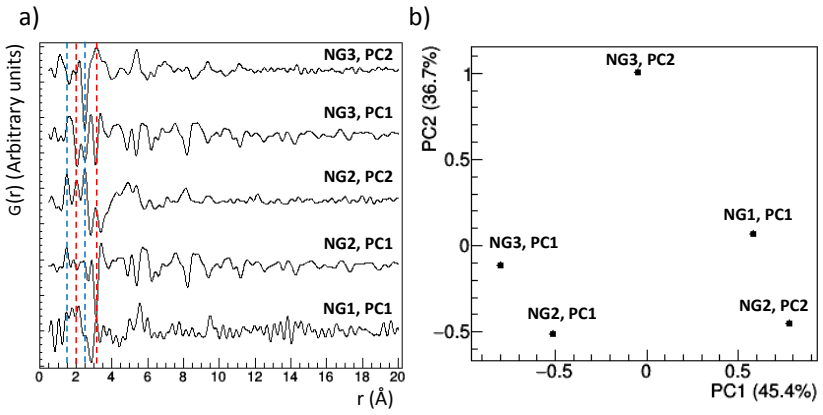

Figure 18 PCA comparison among loading values obtained by PCA applied to PDF profiles without background subtraction from *operando* measurements in a single voltammetry cycle on the three NiGraf samples. a) Loadings profiles considered, shifted relative to each other and labelled according to the sample and principal component they refer. Dashed lines indicate the relevant interatomic distances from jamborite (red) and GO (blue) crystal phases. b) Score plot indicating how the profiles can be grouped by considering two principal components, which in total describe 82% of the total data variance.

2.8 Potential-dependent principal component analysis

To assess the influence of the electrochemical stimulus on the structure of the nanoparticles, we applied PCA on subsets of *operando* PDF profiles identified along the voltammetric scan. As a first step, this study was performed by considering both voltammetric scans of sample NG2 and NG3, and by dividing the single scans in three subset regions: a) an anodic ramp subset, b) an anodic still

subset and c) a cathodic ramp subset, as visible in Figure 19, where the PCA scores obtained within each subset of profiles are reported using a color scale. No significant results were obtained from the application of the potential-dependent PCA to the NG1 sample, as very limited and statistically irrelevant changes occurred among PDF profiles made within-interval PCA scores.

The most noteworthy peaks were identified at 2.0, 2.5, 3.1, 4.8, 5.3, 6.2, 8.2 Å and 9.3 Å and were highlighted with bars and letters in Figure 19. With reference to Figure 16 and Figure 17, peaks denoted by the letter *c* were associated with Ni-Ni distances of the jamborite phase, peak *b* was associated with the GO phase and peaks *a* have contribution from both the GO phase and Ni-O distances of the jamborite phase. The PCA scores obtained in each interval were corrected for sign ambiguity by considering the sign of the jamborite peaks at 5.3 Å, 8.2 Å and 9.3 Å, all corresponding to distances between further Ni atoms. Results are plotted in Figure 19, where the color threshold change between subsets express a variation between background-subtracted integrated PDF series. This means that the bigger the signal at a certain r for a certain subset, the higher the variation from the precedent subset. Results are similar for the two samples and highlight anti-correlated variations between peak b, from GO, and peaks c from the jamborite Ni-Ni distances. Moreover, it can be noted that for the first CV cycle (segments 0, 1 and 2), NG2 does not show the b signal related to GO, as expected due to the low loading, and signal c is present also in the anodic part of the first voltammetric scan (segment 0).

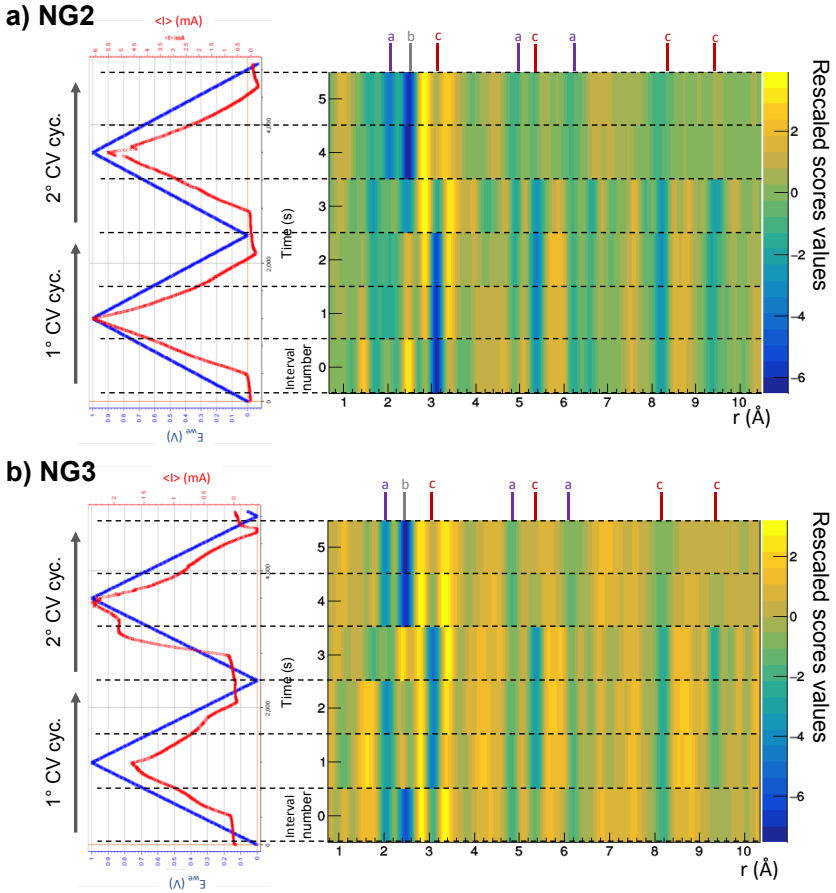

Figure 19 Scores of the potential-dependent PCA during both the CV cycles for the NG2 (a, topmost part) and NG3 (b, bottommost part) NiGraf samples. The left charts depict the potential *E vs.* time (in blue) and the Current *I vs.* time (in red) during voltammety. The two voltammetric cycles for each sample are divided in six intervals of PDF measurements, each interval comprising 12 PDF measurements. The color code for the rescaled score values is shown on the right vertical axis. Signals c are relative to the 3.1 Å, 5.3 Å, 8.2 Å and 9.3 Å PDF Ni-Ni peaks of the jamborite phase, while the b signal at 2.5 Å is associated with the GO phase. Signals a at 2.0 Å, .4.9 Å and 6.2 Å have contribution from both Ni-O jamborite peaks and the GO phase.

On the contrary, for NG3 rgw signal b is clearly visible at lower potentials (segment 0). The second voltammetric cycle on the contrary shows a similar response with respect to PDF between the samples. For both NG2 and NG3, in the initial part of the anodic scan (segment 3) peaks are in line with the ones present in the last segment of the 1st CV cycle (segment 2). Conversely, in the middle and terminal part of the 2nd scan (segments 4 and 5), a strong signal from GO (b) emerges from both samples, which was not present during the first CV, while all the other jamborite signals fade. A fine PDF sampling on the first voltammetric cycle of sample NG3 was also carried out. This time the voltammetric cycle for the NiGraf sample with the highest GO signal due to its higher loading was divided into six different time/potential ranges, each one comprising 6 PDF measurements covering 400 s of the voltammetric scan and defining three potential ranges for the half scan: a) from 1.06 V to 1.40 V, b) 1.40 V to 1.74 V and c) from 1.73 V to 2.06 V.

The first three ranges could be thus associated with the anodic (forward) scan, and the last three with the backward (cathodic) scan. The rescaled values of the PCA scores calculated in each interval are shown in Figure 20.

Therein peaks a, due to the Ni-O distances from the jamborite phase and C-C distances from the GO phase, do not seem to change with the voltammetric scan, while peak b and peaks c change their intensity in the different potential ranges. It may be noted how changes in peaks c are always correlated, as they correspond to Ni-Ni distances, while they appear to be anti-correlated with changes in peak b, which correspond to GO interchain distances. In the most anodic part of the scan (Figure 20, ranges 3, 4 and 5) one can notice an increase in the intensities of peaks c, and a decrease of that of peak b. On the other hand, while for ranges 1, 2 and 6 in the most cathodic regions, an increase in b is visible, along the decrease in c. Moreover, a splitting in b is observed at the highest oxidative potentials (range 4).

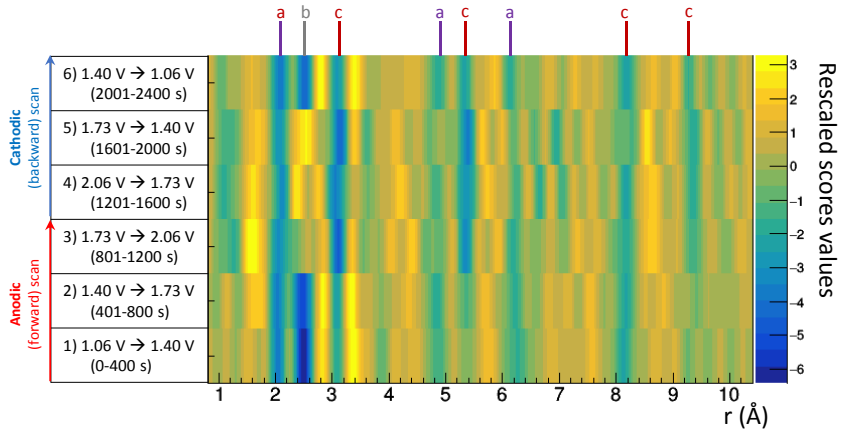

Figure 20 Scores of the potential-dependent PCA during the first CV cycle of the NG3 NiGraf sample. The voltage values and time during the CV scan corresponding to the six intervals of PDF measurements are shown on the left vertical axis. Each interval comprises 6 PDF measurements. The color code for the rescaled score values is shown on the right vertical axis. Signals c are relative to the 3.1 Å, 5.3 Å, 8.2 Å and 9.3 Å PDF Ni-Ni peaks of the jamborite phase, while the b signal at 2.5 Å is associated with the GO phase. Signals a at 2.0 Å, .4.9 Å and 6.2 Å have contribution from both Ni-O jamborite peaks and the GO phase.

3. DISCUSSION

In brief, the analysis of *operando* X-ray diffraction data applied to the new NiGraf electrocatalyst [19] has validated PCA as an effective approach for extracting trends from data. Similar trends are obtained by using XRPD or PDF profiles, suggesting that the Fourier transform does not obscure any details within the data. Consequently, the evolution of the system during the experiment can equivalently be studied in reciprocal or direct space. Notably, it has been demonstrated that the primary limiting factor for *operando* experiments with low signal-to-background ratio, such as those utilizing an electrochemical cell, is the loss of coherence between successive profiles. Hence, experimental conditions need to ensure that any variation between two successive measurements is exclusively caused by

alterations in the sample itself. In our study, this requirement was not met under certain conditions. Specifically, this occurred when conducting *operando* measurement in the XRPD setup, where the detector was positioned 1.411 meters away from the sample (Figure S3). Additionally, this condition was not fulfilled when subtracting the background from individual profiles through offline analysis, especially when the signal from active atoms was very faint, as for the NG1 sample (Figure S5).

While trends in data can be equivalently extracted by analysing XRPD or PDF profiles, the ability to interpret such changes leans decisively towards the PDF. When XRPD profiles are collected in a PDF setup, meaning with high energy of the primary beam and the detector at only 243 mm downstream the sample, they suffer from low angular resolution and are often dominated by background from diffuse scattering. Consequently, Bragg peaks strongly overlap and become difficult to identify. In these conditions, recognizing structural variations of crystalline phases becomes difficult. Conversely, PDF profiles, which encode information on the local structure, are better suited for interpretating structural changes caused by active atoms and distinguishing them from contribution from bulk and "silent" atoms. Moreover, PDF profiles are highly valuable for discerning significant components in PCA, as they have specific features characterizing their envelope and power spectrum. Thus, components loadings showing a stronger contribution from high frequencies, like those shown in Figures S4 and S5, can be deemed insignificant.

The interpretation of loadings obtained by applying PCA to PDF *operando* measurements in terms of structural features was facilitated by prior static measurements on the same NiGraf samples [19]. In said previous measurements, samples were characterized in terms of crystal phase identification and structural fitting. This prior characterization enabled us to interpret the loadings by leveraging the fact that the PDF profiles of the two crystal phases present in the samples have well-defined and separated characteristic peaks, located in the first 3.2 Å interatomic distances (Figure 16). Two pairs of peaks were assigned to jamborite and GO phases. This assignment guided our interpretation of the loading values obtained through the PCA analysis.

The MED framework did not strictly apply for all samples, due to the simultaneous contributions of two active atoms: one from the jamborite phase, the other from the GO phase. While the applied voltage induces a change in the oxidation state of the Ni atoms in jamborite, transitioning from Ni^{2+} to Ni^{3+}, it also triggers a structural alteration in both the metal and carbon phases, affecting the mutual distance among carbon chains stacked along the *c* axis, and the Ni-Ni distances. Moreover, the complexity of the system's response results in variability in the order of principal components holding the relevant MED information, which must be identified on a case-by-case basis. Analysis of loadings shows that changes in the two phases are in counterphase, as indicated by their corresponding PDF peaks having opposite sign in the loadings (

Figure ***14***,

Figure ***15*** and Tables S1, S2).

These conclusions are reinforced by the comparative analysis of the loadings derived from processing the PDF profiles collected during a single voltammetry cycle for the three samples (Figure 18). Within the framework of the MED theory,

this analysis can be interpreted as follows: the PC1 loadings from NG2 and NG3 are connected to the mixed-atom contribution (active + silent atoms), and they are dominated by characteristic PDF peak at 3.1 Å of the jamborite phase. On the contrary, the PC2 loadings from the same samples are linked to the active atom contribution, predominately featuring the PDF peak at 2.5 Å of the GO phase.

It is noteworthy that the interatomic distances of the two crystal phases involved in the structural changes are not those within the first coordination shell. The shortest distances, such as Ni-O (PDF peak at 2.0 Å) for jamborite and C-C (PDF peak at 1.5 Å) for GO, are not featured prominently in the loadings profiles attributed to active atoms. These distances are strongly constrained by chemical bond, which remains relatively unperturbed by the *in situ* electrochemical stimulus. Instead, the most significant contribution to the MED signal arises from the PDF peak at 2.5 Å of the GO phase, corresponding to an interatomic distance associated to crystal packing. This observation suggests that the electrochemical stimulus primarily affects weaker intermolecular interactions rather than the stronger intramolecular ones, resulting in structural changes that are evident prominently in the PDF profiles. The method of the potential-dependent PCA applied to PDF profiles confirms this trend, and shows another interesting characteristic of this novel molecularly doped metal. The peaks from the GO phase and the Ni- Ni jamborite phase intensify in counterphase with respect to each other. This is evident both from Figure 19 and Figure 20. Particularly, from Figure 20, at lower potentials (below OER potentials) the peak related to GO entities distances (2.5 Å) remains clearly visible, and fades in intensity at higher oxidative potentials, returning to its original state during the backward voltammetric scan. This suggests a loss in order in the GO phase at the potentials in which the OER occurs, which is reversibly re-acquired when the potentials are brought back to the initial values. On the other hand, the signals associated with different Ni-Ni distances in the jamborite phase (peaks c in in Figure 19 and in Figure 20), nearly absent at lower potentials, strengthen in the ranges in which higher oxidative potentials are applied. All this happens while the signals a, representative of the Ni-O distance and more distant C-C atoms in GO remain unaffected by the applied potential stimulus.

Weakening of the Ni-Ni signal from the PCA scores in the 2nd scan of NiGraf samples NG2 and NG3 displayed in Figure 19, was investigated by studying the evolution of the PDF profiles during the two-cycle *in situ* experiments (Figure S9). It can be noted that peaks become narrower and sharper as the experiment progresses, following a continuous trend *not* correlated with voltage variations, which could be related to the monotonic trend obtained for the PC1 scores in most of the PCA performed on these metal organic alloy (MORAL) samples. Moreover, Figure S9 shows that this evolution reaches a *plateau* for the PDF profiles collected during the decrease of potential in the 2nd scan. These PDF profiles seem to vary less than in the other regions, and this is the reason why the differential analysis performed by the voltage-dependent PCA affords weaker signals in the intervals 4 and 5 of Figure 19. This quenching of the structural signal from X-rays is accompanied by a stronger measured current. Hence, this effect is likely due to a stabilization of the NiGraf electrocatalyst, which emerges from the initial transient phase characterized by important structural changes. The stabilization phase is probably related to the activation of the catalyst itself, which has to incur into oxidative stress in order to prepare its NiOOH surface toward electrochemical oxidation [30].

4. CONCLUSIONS

Operando PDF experiments using electrochemical cells pose challenges due to significant background contributions that vary throughout the experiment. This difficulty is particularly pronounced when the catalytic material is deposited in the cell as an "ink" on a conductive support. Under such conditions, surface electrochemical effects may dominate, distinct from the bulk material that is not actively participating in the reaction.

Our study provides a protocol for optimizing such experiments, which includes both the experimental setup and the data analysis. From the experimental point of view, we have demonstrated that by simply making a hole in the conductive carbon support it is possible to improve the signal-to-noise ratio and eliminate structured background contributions with a minor loss in electrochemical signal. A careful alignment of the cell, which can be monitored by collecting XRPD data by changing the position of the empty cell, makes it possible to center the X-ray beam on the aperture. In addition, we found that the typical PDF setup, with the detector very close to the sample, minimizes the fluctuations of the diffraction signal due to scattering of air or sampling different regions of the detector. Accordingly, we were able to extract regular trends in data by processing the PDF measurements, from which the response of the system can be monitored. Conversely, no discernible trend in the data could be identified through analysis of XRPD measurements, necessitating placement of the detector at a considerable distance from the sample.

This new experimental and computational crystallographic protocol involves the use of PCA scores (calculated from XRPD or PDF profiles) to recognize the MED quadratic relationship and identify the candidate principal components holding the signal from active atoms. Then PCA loadings calculated from PDF profiles are used to check the significance of the principal components, by comparison with the features of an ideal PDF profile; and to infer changes in the local structure that are responsible for the trend in data captured by the given principal component.

From the computational point of view, we demonstrate that PCA is a valid tool for the fast monitoring of data during the execution of the experiment and to highlight differences in data. With this tool, we identified a consistent trend by analyzing data through PCA in reciprocal space (XRPD profiles) or in direct space (PDF profiles calculated from the previous XRPD profiles), thus proving that calculation of total scattering and Fourier transform do not introduce artifacts in the PDF profiles.

In case of two voltammetric cycles, we show that the system response can be captured by different principal components in the two cycles. Moreover, the application of MED analysis to our MORAL samples is not straightforward because: *i*) for NG1 NiGraf sample the structural changes of the unique phase present (jamborite) are limited, so that only one principal component is significant; and *ii*) for NG2 and NG3 NiGraf materials two types of active atoms, arising from the two crystal phases (GO and jamborite) are present, and their changes are captured by the same principal component.

A very interesting result from the catalysis viewpoint was obtained when studying the correlation between the electrochemical and the structural response of the molecularly doped metal. For the NiGraf sample with the highest loading of GO, the variation in score values from the potential-dependent PCA of the *in situ* PDF profiles reveals a distinct and reversible trend during the initial voltammetric cycle. Specifically, the signal from the GO intensifies at higher oxidative potentials. On the other hand, at lower potentials, the signal related to the jamborite Ni-Ni bond grows in intensity at the beginning and at the end of the first cycle, and it is heavily reduced after the second cycle. This could indicate a stabilization of the active phase of the catalyst (the activation of the catalyst itself) which follows a transient

regime dominated by a crosstalk between the jamborite and GO phases. This unique synergistic effect most likely arises from the 3D entrapment of GO within the jamborite nanocrystallites structural characteristic of MORALs [31], which is completely different from 2D surface-decorated GO/Ni electrocatalysts [17,32].

5. EXPERIMENTAL METHODS

5.1 Sample preparation

The NiGraf samples analyzed in this study are reported in Table 1. They have been synthesized as previously reported [19]. The NiOx particles have a dimension between 50 and 100 nm. Graphene oxide in aqueous solution (8 mg/mL, product code NG01GO0501) was purchased from Nanografi Nano Technology (Çankaya/Ankara, Türkiye). The solution consists of 1-5 μm large GO microparticles varying in thickness between 0.4 and 1.1 nm [33].

Table 1. NiGraf sample name and GO load.

Name	Go load (wt %)
NG1	0.2
NG2	1.0
NG3	5.0

5.2 The electrochemical experiment

The electrochemical cell has been specifically designed to carry out *operando* PDF measurements. The sample is mounted on the cell with this procedure: first a ink is prepared by mixing 2 mg of the powdered sample with 500 μl water, 500 μL ethanol and few drops of Nafion ionomer. Then the ink is sonicated for 20 min, and 200 μL were dropcasted on the pin-holed exposed part of the carbon paper previously inserted in the cell. It was let dry and finally the cell was closed with the other kapton window. For the electrochemical measurements, a Pt wire was used as counter electrode, while an Ag/AgCl/KCl Sat. electrode was used as reference electrode. All the potentials are expressed *vs.* reversible hydrogen electrode (RHE). *In situ and operando* measurements were performed using an electrolytic solution of 1M KOH (Sigma Aldrich) in Milli-Q water, while a Biologic VSP-300 potentiostat was used to control the experiments. The single voltammetries of each electrocatalyst are coupled with the voltammetry of the pin-holed carbon paper (CP) substrate, acquired using the same experimental set-up, in order to highlight the small Influence of the substrate on the overall OER electrochemistry. Prior to the PDF voltammetric cycle, 10 CV scans in the range (1 to 1.6 V vs. RHE, using a scan speed of 50 mV/sec have been performed to condition the working electrode.

5.3 PDF measurements

PDF profiles were collected at the 28ID-2 beamline of the National Synchrotron Light Source (NSLS-II) of the Brookhaven National Laboratory, USA, with an X-ray energy of 68.36 keV (0.1814 Å) and a 0.5 mm × 0.5 mm beam size. Measurements were performed in transmission mode and at room temperature. The beamline is equipped by two Perkin Elmer XRD 1621 digital imaging detectors, each consisting of a flat scintillator panel CsI coated, whose active area is formed by 2048 × 2048 pixels with size 200 × 200 μm. They were mounted

orthogonal to the beam path, at 243 mm and 1411 mm downstream of the sample, according to a setup optimized for PDF and XRPD measurements, respectively. Static measurements were carried by filling Lindemann capillaries with powder samples. An empty capillary was measured for background estimation and cerium oxide was measured as a standard material to calibrate the wavelength and the detector position. *Operando* measurements were carried out by mounting the electrochemical cell perpendicular to the beam, as shown in

Figure 2. Each measurement takes 1 min (45 s acquisition time + 15 s dead time). Three subsequent background measurements were taken in the same conditions, and then averaged. The potential to the electrodes was supplied on-site by a Biologic BCS-810 potentiostat positioned outside the experimental hutch. The cell without sample, but filled with the electrolytic solution, was used measured for background estimation. Measurements were carried out at different cell positions, and, for each position, three images were acquired and averaged, to increase the signal over background ration.

5.4 X-rays data analysis

Diffraction images were azimuthally integrated and converted into intensity XRPD profiles vs momentum transfer $q = 4\pi\sin\theta/\lambda$ by using the DIOPTAS program [34]. PDF profiles were calculated from the q profiles with the program PDFGetX3 [35]. The parameters for PDF calculation (background subtraction, scale factor, minimum and maximum values of q, degree of data-correction polynomial) were optimized on individual PDF profiles, to avoid large termination effects and preserve the signal to noise ratio. The q_{max} values used for PDF generation are listed in Tables S1, S2 and S3 for respectively NG1, NG2 and NG3 samples. The collected patterns and the PDF profiles were compared by principal component analysis (PCA) by using the RootProf program [36,37]. PCA loadings obtained from PDF data were fitted with structural models by using the program PDFgui [38].

A potential-dependent variant of PCA was implemented in the program RootProf, according to the following protocol: several PCA runs are performed sequentially on subsets of the measured profiles, identified by considering the trend of the potential applied in the voltammetric cycles. The score values obtained by PCA applied on each subset of measurements are corrected for the sign ambiguity, rescaled by a standard normal variate transformation, i.e. subtracted by their mean and divided by their standard deviation, and plotted as a function of the interval number. The protocol adopted for the potential-dependent PCA is similar that developed for the space-dependent PCA applied in [39].

5.5 The MED theory

Modulation Enhanced Diffraction (MED) is a technique that allows a selective detection of active atoms by the analysis of *operando* X-ray diffraction measurements in systems where they are clearly separated from the bulk silent atoms and they belong to a single crystal phase [40]. According to MED predictions, the signal from active atoms can be extracted from data due to its specific behaviour in time domain. In fact, it is expected to vary with time at double the frequency of the stimulus variation. If data are processed by PCA, the signal from active atoms is expected to uniquely contribute to the loadings of a specific principal component, which needs to be identified out of the many components in which data are decomposed by looking at the score values. The MED signal

concerns two principal components (*PCx* and *PCy*) linked by a quadratic relationship among their scores value, i.e.

$$Scores_{PCy} = Scores_{PCx} * Scores_{PCx} \quad (1)$$

Once the components that follows eq. (1), even approximately, are identified, the signal from active atoms is expected to uniquely contribute to the loadings of the component *PCy*. In case of active atoms belonging to a single crystal phase, the loading values of *PCy* are expected to have a definite sign and represent the X-ray profile from active atoms only [20].

DATA AVAILABILITY STATEMENT

The data that support the findings of this study are available from the corresponding author upon reasonable request.

ACKNOWLEDGMENTS

This research was funded by the European Union – NextGenerationEU from the Ministero dell'Ambiente e della Sicurezza Energetica POR H2 AdP MMES/ENEA with involvement of CNR and RSE, PNRR - Mission 2, Component 2, Investment 3.5 "Ricerca e sviluppo sull'idrogeno", CUP: B93C22000630006. Rocco Lassandro (CNR-IC) is gratefully acknowledged for its support in carrying out the synchrotron measurements at BNL. The access to the National Synchrotron Light Source (Brookhaven National Laboratory, NY, US) was supported by the U.S. Department of Energy, Office of Science, Office of Basic Energy Sciences, under Contract No. DE-SC0012704 (NSLS-II Proposal Number 312211). Enrico Berretti would like to acknowledge the Made in Italy - Circular and Sustainable (MICS) Extended Partnership funded by the European Union - NextGenerationEU (Piano Nazionale di Ripresa e Resilienza (PNRR) - Missione 4, Componente 2, Investimento 1.3 – D.D. 1551.11-10-2022, PE00000004) for financial support. Authors would like to acknowledge Carlo Bartoli from the ICCOM-CNR workshop for the electrochemical cell production and design.

DECLARATION OF INTERESTS

The authors declare no competing interests.

REFERENCES

1. B. Roldán Cuenya, M. A. Bañares, Introduction: *operando* and *in situ* studies in catalysis and electrocatalysis, Chem. Rev. 124 (2024) 8011–8013. DOI: 10.1021/acs.chemrev.4c00184
2. I. Neumann, B. Rasche, *In situ* diffraction in electrochemistry – A practical introduction for experiments beyond batteries, Curr. Op. Electrochem. 39 (2023) 101288. DOI: 10.1016/j.coelec.2023.101288
3. O. J. Borkiewicz, B. Shyam, K. M. Wiaderek, C. Kurtz, P. J. Chupas, K. W. Chapman, The AMPIX electrochemical cell: a versatile apparatus for *in situ* X-ray scattering and spectroscopic measurements, J. Appl. Cryst. 45 (2012) 1261–1269. DOI: 10.1107/S0021889812042720
4. M. J. Young, M. N. M. Bedford, N. Jiang, D. Lin, L. Dai, *In situ* electrochemical high-energy X-ray diffraction using a capillary working electrode cell geometry, J. Synchrotron Rad. 24 (2017) 787–795. DOI: 10.1107/S1600577517006282
5. M. D. Lopez, G. L. Cutts, P. K. Allan, D. S. Keeble, A. Ross, V. Pralong, G. Spiekermanne, P. A. Chatera, Fast *operando* X-ray pair distribution function using the DRIX electrochemical cell, J. Synchrotron Rad. 27 (2020) 1190–1199. DOI: 10.1107/S160057752000747X
6. R. Ciriminna, M. Pagliaro, Enhanced nickel catalysts for producing electrolytic hydrogen, RSC Sustainability 1 (2023) 1386-1393. DOI: 10.1039/d3su00177f
7. L. Huo, C. Jin, K. Jiang, Q. Bao, Z. Hu, J. Chu, Applications of nickel-based electrocatalysts for hydrogen evolution reaction, Adv. Energ. Sus. Res. 3 (2022) 2100189. DOI: 10.1002/aesr.202100189
8. S.A.S. Machado, L.A. Avaca, The hydrogen evolution reaction on nickel surfaces stabilized by H-absorption, Electrochim. Acta 39 (1994) 1385-1391. DOI: 10.1016/0013-4686(94)E0003-I
9. K. Juodkazis, J. Juodkazytė, R. Vilkauskaitė, V. Jasulaitienė, Nickel surface anodic oxidation and electrocatalysis of oxygen evolution, J. Solid State Electr. 12 (2008) 1469–1479. DOI: 10.1007/s10008-007-0484-0
10. Y. Chen, K. Rui, J. Zhu, S. X. Dou, W. Sun, Recent progress on nickel-based oxide/(oxy)hydroxide electrocatalysts for the oxygen evolution reaction, Chem. Eur. J. 25 (2018) 703-713. DOI: 10.1002/chem.201802068
11. H. A. Miller, K. Bouzek, J. Hnat, S. Loos, C. I. Bernäcker, T. Weißgärber, L. Röntzsch. J. Meier-Haack, Green hydrogen from anion exchange membrane water electrolysis: a review of recent developments in critical materials and operating conditions, Sustain. Energy Fuels 4 (2020) 2114-2133. DOI: 10.1039/C9SE01240K
12. C. Santoro, A. Lavacchi, P. Mustarelli, V. Di Noto, L. Elbaz, D. R. Dekel, F. Jaouen, What is next in anion-exchange membrane water electrolyzers? Bottlenecks, benefits, and future, ChemSusChem 15 (2022) e202200027. DOI: 10.1002/cssc.202200027
13. Q. Hassan, A. Z. Sameen, H. M. Salman, M.Jaszczur, Large-scale green hydrogen production via alkaline water electrolysis using solar and wind energy, Int. J. Hydrogen Energ. 48 (2023) 34299-34315. DOI: 10.1016/j.ijhydene.2023.05.126.
14. H. Radinger, P. Connor, S. Tengeler, R. W. Stark, W. Jaegermann, B. Kaiser, Importance of nickel oxide lattice defects for efficient oxygen evolution reaction, Chem. Mater. 33 (2021) 8259–8266. DOI: 10.1021/acs.chemmater.1c02406
15. H. Wang, J. Xue, C. Liu, Z. Chen, C. Li, X. Li, T. Zheng, Q. Jiang, C. Xia, CO_2 electrolysis toward acetate: A review, Curr. Op. Electrochem. 39 (2023) 101253. DOI: 10.1016/j.coelec.2023.101253
16. Y. Zhao, J. You, L. Wang, W. Bao, R. Yao, Recent advances in Ni_3S_2-based electrocatalysts for oxygen evolution reaction, Int. J. Hydrogen Energ. 46 (2021) 39146-39182. DOI: 10.1016/j.ijhydene.2021.09.137

17. X. Han, N. Suo, C. Chen, Z. Lin, Z. Dou, X. He, L. Cui, Graphene oxide guiding the constructing of nickel-iron layered double hydroxides arrays as a desirable bifunctional electrocatalyst for HER and OER, Int. J. Hydr. Energy 44 (2019) 29876-29888. DOI:10.1016/j.ijhydene.2019.09.116
18. A. Zhou, J. Bai, W. Hong, H. Bai, Electrochemically reduced graphene oxide: Preparation, composites, and applications, Carbon 191 (2022) 301-332. DOI:10.1016/j.carbon.2022.01.056
19. M. Pagliaro, M. V. Pagliaro, R. Caliandro, C. Giannini, R. Ciriminna, A. Lavacchi, NiGraf: a new nickel-based molecularly doped metal for enhanced water electrolysis, Mater. Adv. 5 (2024) 2759-2766. DOI: 10.1039/d3ma00700f
20. D. Chernyshov, W. Van Beek, H. Emerich, M. Milanesio, A. Urakawa, D. Viterbo, L. Palin, R. Caliandro, Kinematic diffraction on a structure with periodically varying scattering function, Acta Crystallogr. A 67 (2011) 327-335. DOI:10.1107/S0108767311010695
21. R. Caliandro, D. Chernyshov, H. Emerich, M. Milanesio, L. Palin, A. Urakawa, W. van Beek, D. Viterbo, Patterson selectivity by modulation-enhanced diffraction J. Appl. Crystallogr. 45 (2012) 458-470. DOI:10.1107/S0021889812011569
22. E Berretti, M.V. Pagliaro, A. Giaccherini, G. Montegrossi, F. Di Benedetto, G.O. Lepore, F. D'Acapito, F. Vizza, A. Lavacchi, Experimental evidence of palladium dissolution in anodes for alkaline direct ethanol and formate fuel cells, Electrochim. Acta 418 (2022) 140351. DOI:10.1016/j.electacta.2022.140351
23. E. Berretti, A. Giaccherini, G. Montegrossi, F. D'Acapito, F. Di Benedetto, C. Zafferoni, A. Puri, G. O. Lepore, H. Miller, W. Giurlani, M. Innocenti, F. Vizza, A. Lavacchi, *In-situ* quantification of nanoparticles oxidation: a fixed energy X-ray absorption approach, Catalysts 9 (2019) 659. DOI: 10.3390/catal9080659
24. G. Montegrossi, A. Giaccherini, E. Berretti, F. Di Benedetto, M. Innocenti, F. d'Acapito, A. Lavacchi, Computational speciation models: a tool for the interpretation of spectroelectrochemistry for catalytic layers under operative conditions, J. Electrochem. Soc. 164 (2017) E3690. DOI: 10.1149/2.0711711jes
25. R. B. Neder, T Proffen Exact and fast calculation of the X-ray pair distribution function, J. Appl. Cryst. 2020, 53, 710–721. DOI: 10.1107/S1600576720004616
26. K W. Chapman, S. H. Lapidus, P. J. Chupas, Applications of principal component analysis to pair distribution function data, J. Appl. Crystallogr. 48 (2015) 1619–1626. DOI: 10.1107/S1600576715016532
27. R. Caliandro, P. Guccione, G. Nico, G. Tutuncu, J.C. Hanson, Tailored multivariate analysis for modulated enhanced diffraction, J. Appl. Crystallogr. 48 (2015) 1679-1691. DOI: 10.1107/S1600576715017070
28. P. Guccione, M. Lopresti, M. Milanesio, R. Caliandro Multivariate analysis applications in x-ray diffraction, Crystals 11 (2020) 12 DOI: 10.3390/cryst11010012
29. O. Diaz-Morales, D. Ferrus-Suspedra, M. T. M. Koper, The importance of nickel oxyhydroxide deprotonation on its activity towards electrochemical water oxidation, Chem. Sci. 7 (2016) 2639-2645. DOI: 10.1039/c5sc04486c
30. S. Klaus, Y. Cai, M. W. Louie, L. Trotochaud, A. T. Bell, Effects of Fe electrolyte Impurities on Ni(OH)2/NiOOH structure and oxygen evolution activity, J. Phys. Chem. C 119 (2015), 7243–7254 DOI: 10.1021/acs.jpcc.5b00105
31. D. Avnir, Recent progress in the study of molecularly doped metals, Adv. Mater. 30 (2018) 1706804. DOI: 10.1002/adma.20170680430
32. A. V. Munde, B. B. Mulik, P. P. Chavan, B. R. Sathe, Enhanced electrocatalytic activity towards urea oxidation on Ni nanoparticle decorated graphene oxide nanocomposite, Electrochim. Acta 349 (2020) 136386. DOI: 10.1016/j.electacta.2020.136386

33. Nanografi Nano Technology, Graphene Oxide Water Dispersion 8 mg/mL, https://nanografi.com/graphene/graphene-oxide-dispersion-8-mg-ml-in-h2o/ (accessed July 11, 2024)
34. C. Prescher, V.B. Prakapenka, DIOPTAS: a program for reduction of two-dimensional X-ray diffraction data and data exploration, High Pres. Res. 35 (2015) 223-230. DOI: 10.1080/08957959.2015.1059835
35. P. Juhás, T. Davis, C. L. Farrow, S. J. L. Billinge, PDFgetX3: a rapid and highly automatable program for processing powder diffraction data into total scattering pair distribution functions, J. Appl. Crystallogr. 46 (2013) 560–566. DOI: 10.1107/S0021889813005190
36. R. Caliandro, B. D. Belviso, RootProf: software for multivariate analysis of unidimensional profiles, J. Appl. Cryst. 47 (2014) 1087-1096. DOI: 10.1107/S1600576714005895
37. A. Mazzone, M. Lopresti, B.D. Belviso, R. Caliandro, New features of the RootProf program for model-free analysis of unidimensional profiles, J. Appl. Crystallogr. 56 (2023) 1841-1854. DOI: 10.1107/S1600576723008348
38. C. L. Farrow, P. Juhás, J. W. Liu, D. Bryndin, E. S. Božin, J. Bloch, T. Proffen, S.J.L. Billinge, PDFfit2 and PDFgui: computer programs for studying nanostructure in crystals, J. Phys. Condens. Matter 19 (2007) 335219. DOI: 10.1088/0953-8984/19/33/335219
39. R. Caliandro, D. Altamura, B.D. Belviso, A. Rizzo, S. Masi, C. Giannini, Investigating temperature-induced structural changes of lead halide perovskites by *in situ* X-ray powder diffraction, J. Appl. Crystallogr. 52 (2019) 1104-1118. DOI: 10.1107/S160057671901166X
40. L. Palin, R. Caliandro, D. Viterbo, M. Milanesio Chemical selectivity in structure determination by the time dependent analysis of *in situ* XRPD data: a clear view of Xe thermal behavior inside a MFI zeolite, Phys. Chem. Chem. Phys. 17 (2015) 17480-17493. DOI: 10.1039/C5CP02522B